Eur. Phys. J. Plus (2024) 139:928
https://doi.org/10.1140/epjp/s13360-024-05719-6

THE EUROPEAN
PHYSICAL JOURNAL PLUS

Regular Article

X-ray science using the ESRF—extremely brilliant source

Patrick Bruno[1,a], **Jean-Claude Biasci**[1,b], **Carsten Detlefs**[1,c], **Rudolf Dimper**[1], **Michael Krisch**[1,d], **Gema Martínez-Criado**[1,e], **Mohamed Mezouar**[1,f], **Christian Nevo**[1,g], **Qing Qin**[1,h], **Pantaleo Raimondi**[1,2,i], **Harald Reichert**[1,3,j], **Francesco Sette**[1,k], **Jean Susini**[1,4,l], **Paul Tafforeau**[1,m], **Can Yildirim**[1,n]

[1] ESRF-The European Synchrotron, 71 avenue des Martyrs, Grenoble 38000, France
[2] Present Address: Fermilab, PO Box 500, Batavia, IL 60510-5011, USA
[3] Present Address: Deutsches Elektronen-Synchrotron DESY, Notkestr. 85, Hamburg 22607, Germany
[4] Present Address: Synchrotron SOLEIL, L'Orme des Merisiers, Départementale 128, Saint-Aubin 91190, France

Received: 13 May 2024 / Accepted: 27 September 2024

Abstract The Extremely Brilliant Source (EBS), the first high-energy 4th-generation synchrotron radiation source, constructed at the ESRF and based upon the novel concept of a Hybrid Multi-Bend Achromat (HMBA), has started user operation on August 25th, 2020. We report here on selected recent scientific results exploiting the greatly improved performances of this novel X-ray source.

1 Introduction to the facility

The European Synchrotron Radiation Facility (ESRF), located in Grenoble, France, is a high-energy (6 GeV) electron storage ring, producing highly brilliant X-ray radiation. It was founded in 1988, as a joint collaboration of 11 European Countries, and was the world's first 3rd-generation synchrotron radiation source based upon the concept of a Double-Bend Achromat (DBA), producing high-brilliance radiation from insertion devices (undulators) [1]. The first X-rays were produced in 1992, and the ESRF opened for user operation in 1994 with 15 beamlines. Detailed historical accounts of the scientific, technological, and international aspects of the creation of the ESRF are given in Ref. [2] and [3], respectively.

Today, the number of participating countries has grown to 21 (13 Members and 8 Scientific Associates), with a capacity of 51 beamlines (37 ESRF beamlines and 14 Collaborating Research Groups (CRG) beamlines), including two cryogenic electron microscopes (cryo-EM) (1 ESRF and 1 CRG).

Over the past 30 years, the ESRF has enabled major scientific breakthroughs in the understanding of living and condensed matter. Scientists from all over the world have access to beamtime on the basis of scientific excellence.

Starting in 2007, the ESRF initiated a significant upgrade of its experimental infrastructure. Phase I (2008–2015) involved a thorough modernization of its beamlines portfolio, accompanied by the construction of new extension facilities. These developments facilitated the construction of long beamlines capable of delivering nanoscale X-ray beams, thereby enhancing the facility's capabilities in various domains, including nanosciences, nanotechnology, pump-probe experiments, time-resolved sciences, structural and functional biology, soft matter research, and X-ray imaging [4].

---

[a] e-mail: patrick.bruno@esrf.fr (corresponding author)
[b] e-mail: biasci@esrf.fr
[c] e-mail: detlefs@esrf.fr
[d] e-mail: krisch@esrf.fr
[e] e-mail: gema.martinez@esrf.fr
[f] e-mail: mezouar@esrf.fr
[g] e-mail: christian.nevo@esrf.fr
[h] e-mail: qing.qin@esrf.fr
[i] e-mail: praimond@fnal.gov
[j] e-mail: harald.reichert@desy.de
[k] e-mail: sette@esrf.fr
[l] e-mail: jean.susini@synchrotron-soleil.fr
[m] e-mail: paul.tafforeau@esrf.fr
[n] e-mail: can.yildirim@esrf.fr

Phase II of the ESRF upgrade program (2015–2023) entailed the replacement of the original 3rd-generation radiation source, by a completely new source, the "Extremely Brilliant Source," based upon the concept of a Hybrid Multi-Bend Achromat (HMBA) [5, 6], with considerably improved performances, in particular with the reduction of the horizontal emittance by a factor 30, leading to an increase of the brilliance and transversal coherence by a factor 100.

The new source is described briefly in Sect. 2, whereas the current beamline portfolio is outlined in Sect. 3. Next, Sect. 4 is devoted to the presentation of some selected results, showcasing the considerable improvement generated by the EBS, in various fields of science. Finally, Sect. 5 addresses the perspective and new challenges to be tackled at the ESRF in the coming years.

2 The extremely brilliant source

The original ESRF source was a 6 GeV storage ring of 844 m circumference, comprising 32 cells, based upon the concept of Double-Bend Achromats. The horizontal and vertical beam emittances were, respectively, $\epsilon_x = 4$ nm·rad and $\epsilon_z = 4$ pm·rad, resulting in a highly anisotropic beam shape. The large horizontal emittance results in an inefficient use of the emitted photons, and is the most serious limiting factor of progress in applications requiring high-flux beams of nanometer size, or for applications exploiting the transverse coherence of the photon beam. Furthermore, the highly anisotropic shape of the X-ray beam results in severe limitations for the design of experiments (optics, etc.).

The EBS was conceived at ESRF in 2013 as a new concept, which enables to overcome the obstacles to reduce the beam emittance under the constraints of maintaining the electron beam energy (6 GeV), the ring circumference (844 m), and preserving the existing accelerator tunnel, as well as the insertion devices and beamlines.

In-depth studies have shown that those constraints did not allow a significant increase of the source performances by improving the existing source concept (DBA).

In order to mitigate these difficulties, the EBS lattice is based on a variation of the Standard Multi-Bend Achromat [7, 8]. The layout is referred to as a Hybrid Multi-Bend Achromat lattice [9]. The center part of a cell alternates four high-gradient, horizontally focusing quadrupoles and three high-gradient bending magnets, which also provide vertical focusing. The HMBA lattice features a reduction in the number of sextupoles compared to the DBA, with only six sextupoles instead of seven. Additionally, the HMBA design incorporates longer and weaker dipoles, resulting in a decrease in synchrotron radiation. Unlike the 7BA configuration, the HMBA layout eliminates the necessity for large dispersion in the inner dipoles, leading to a significant reduction in the total number of magnets required for the system. At each end of the cell, two dipoles encompass the regions with large β-functions and dispersion. Their longitudinally varying bending field helps to reduce the emittance and increase the dispersion. The lattice functions of the EBS electron beam are shown in Fig. 1. The horizontal and vertical β-functions, β_x and β_z, and the dispersion η_z describe the variation of the horizontal and vertical RMS beam widths, $\sigma_x \equiv \sqrt{\langle x^2 \rangle}$ and $\sigma_z \equiv \sqrt{\langle z^2 \rangle}$ along the ring, in terms of the horizontal and vertical emittances ϵ_x and ϵ_z (which are conserved quantities) as, $\sigma_x^2 = \epsilon_x \beta_x + \eta_x^2 \delta^2$ and $\sigma_z^2 = \epsilon_z \beta_z$. The horizontal and vertical beam emittances of the EBS are $\epsilon_z = 133$ pm·rad and $\epsilon_z = 1$ pm·rad, respectively, whereas the relative energy spread is $\delta = 0.094$ % [11].

Table 1 compares the lattice design parameters between the old ESRF lattice and for the EBS lattice [9]. The size and divergence of the electron beam at source points are listed in Table 2.

Figure 2 (upper panel) shows the brilliance curves for the EBS and for the former ESRF (ESRF 2018) light source. With the same undulators, the brilliance is increased by a factor of 15 at 1 keV, 27 at 10 keV, and 36 at 100 keV.

Together with the increased brilliance, the considerable reduction of the beam emittance increases the coherence of the X-ray beam, as demonstrated by measurements of the Fraunhofer diffraction patterns through horizontal and vertical slits [11], from which the horizontal coherence at 60 m distance from the source was estimated to be $\xi_H = 53.4$ μm at 7.24 keV, and $\xi_H = 19.1$ μm at 20.05 keV, confirming the expected increase of coherent fraction shown in Fig. 2 (lower panel).

The current performance of the EBS is considered to be close to the ultimate performances for a source compatible with the constraints of the ESRF upgrade (beam energy, tunnel, etc.). For a green-field facility, there is significantly more room for performance improvement, and a design for an ultimate, diffraction limited, source (i.e., with emittance $\epsilon_{x,z} < 10$ pm·rad at X-ray wavelength $\lambda = 1$ Å) was recently proposed [13].

3 Beamline portfolio

The ESRF currently operates the equivalent of 32.5 X-ray beamlines, and one cryo-EM (operated jointly with the Institut de Biologie Structurale (IBS) and the European Molecular Biology Laboratory (EMBL)). In addition, the equivalent of 12 CRG beamlines, using bending magnet (BM) sources, and one cryo-EM, are operated by the various member states of the ESRF.

In the phase I of the ESRF upgrade program (2009–2015), a total of 15 new beamlines were constructed and another four beamlines deeply refurbished. In the phase II of the ESRF upgrade program (2015–2023), in addition to the construction of the new source (EBS), and to the refurbishment and upgrade of existing beamlines, four brand new flagship beamlines have been (or are

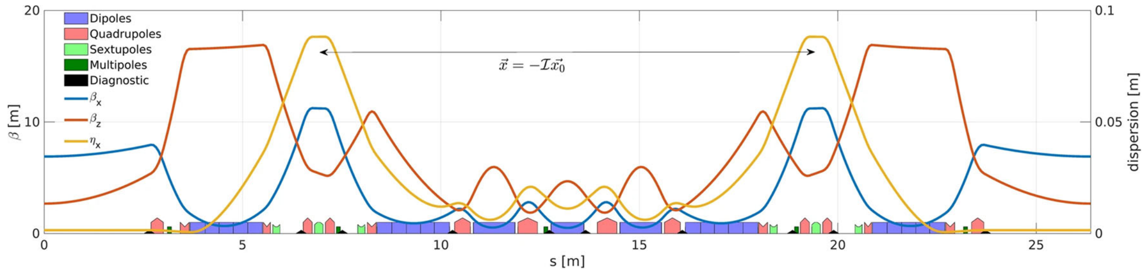

Fig. 1 Lattice functions and magnets layout for the HMBA SR standard cell with two symmetric CCS. Horizontal and vertical steerers and skew quadrupoles are located in each corrector and sextupole depicted in the layout. The β_x, β_z, and η_x Twiss parameters are shown as blue, red, and orange lines, respectively. Reproduced from Ref. [10] under Creative Commons License 4.0 (https://creativecommons.org/licenses/by/4.0/)

Table 1 Lattice design parameters [9]

	ESRF	EBS
Lattice type	DBA	HMBA
Circumference [m]	844.390	843.979
Beam energy [GeV]	6.04	6
Natural emittance [pm]	4000	147
Energy spread [%]	0.106	0.095
Damping times (H/V/L) [ms]	7/7/3.5	8.5/13/8.8
Energy loss per turn [MeV]	4.88	2.60
Tunes (H/V)	36.44/13.39	75.62/27.58
Natural chromaticity (H/V)	−130/−58	−100/−84
Momentum compaction factor	$1.78\ 10^{-4}$	$0.87\ 10^{-4}$

Table 2 Size and divergence of the electron beam at source points (RMS values) [9]

			ESRF (even)	ESRF (odd)	EBS
ID					
	size [μm]	H	388	37.4	27.2
		V	3.46	3.46	3.45
	e-divergence [μrad]	H	10.3	107	5.22
		V	1.15	1.15	1.44
Bending hard					
	size [μm]	H	77.9	112.1	21.3
		V	12.9	11.3	3.74
	e-divergence [μrad]	H	111	98.5	24.2
		V	0.49	0.25	2.96
Bending soft					
	size [μm]	H	98.3	132	14.4
		V	12.8	11.3	4.63
	e-divergence [μrad]	H	116	103	17.8
		V	0.5	0.36	1.52

being) constructed: EBSL1-ID18 (coherent X-rays dynamics and imaging), EBSL2-ID03 (dark-field X-ray microscopy), EBSL3-BM18 (high-throughput large-field phase contrast tomography), EBSL8-ID29 (serial macromolecular crystallography). Finally, the program was completed with the reconstruction of two beamlines (ID14 (nuclear resonance) and ID27 (high pressure)) and the deep refurbishment of another three beamlines (BM05 (instrumentation facility and phase contrast tomography), ID21 (X-ray microscopy), and ID23-1 (macromolecular crystallography)).

The complete list and description of the ESRF beamlines is provided in Supplementary Material Tables S1 to S6; the CRG beamlines are listed in Tables S7 and S8; the plan of ESRF and CRG beamlines is shown in Fig. S1.

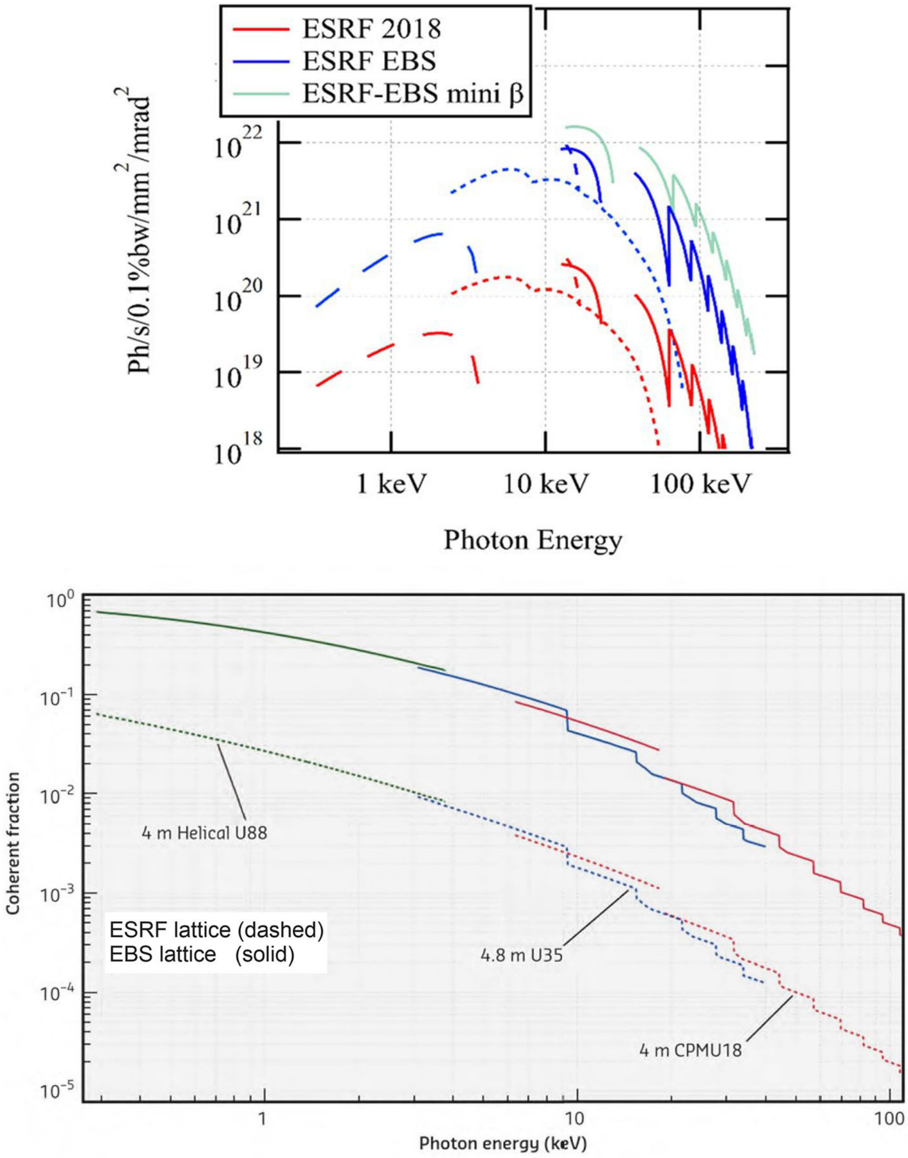

Fig. 2 Upper panel: Brilliance curves for the former ESRF lattice (red), for the EBS lattice (blue) and for a future EBS upgrade with "mini-β" sections and ultra-short-period undulators (green). The dashed curves are for ex-vacuum undulators: 88-mm period, 4-m-long circular polarization undulator at low energy, 35-mm period, 4.8-m-long planar undulator at medium energy, and 20-mm period, 4.8-m-long planar undulator at 14 keV. The solid curves are for 2-m-long cryogenic permanent magnet undulators (CPMUs) with 14.4-mm period for the ESRF DBA and ESRF-EBS, and 12 mm (still to be built and demonstrated) for future mini-β upgrades. Reproduced from Ref. [11] under Creative Commons License 4.0 (https://creativecommons.org/licenses/by/4.0/). Lower panel: Coherent fraction for the former ESRF lattice (dashed lines) and EBS lattice (solid lines). Adapted from Ref. [12] under Creative Commons License 3.0 (https://creativecommons.org/licenses/by/3.0)

4 Selected scientific results obtained with the EBS

In the following, we present a selection of studies performed with the EBS, in three different areas: matter at extreme conditions, dark-field X-ray microscopy, and phase contrast tomography.

4.1 Matter at extreme conditions

Science at extremes conditions of pressure and temperature is a very active field of research. Fundamental questions are addressed in several domains, ranging from condensed-matter physics to Earth and planetary science, as well as material synthesis and characterization, and biology. Applying high pressure at fixed temperature and chemical composition strongly alters interatomic distances, providing a powerful mean to explore free energy landscapes and to search for novel phases of matter.

The new X-ray source provides considerably higher photon flux density and higher transversal coherence, especially for photon energies above 30 keV, i.e., the energy range most relevant for diffraction and imaging at extreme conditions. These improvements enable studies to be carried out on much smaller sample volumes and on much shorter time scales.

The direct impact on studies at extreme conditions is that higher pressure and temperature states, which can only be generated in small volumes or during dynamic, transient processes, become experimentally accessible. In particular, the detailed characterization of material structures and properties (up to pressure values of several TPa, i.e., tens of Mbars) will become possible. This precision will be similar to those currently achieved at 100 GPa by conducting static compression studies using diamond anvil cells and dynamic

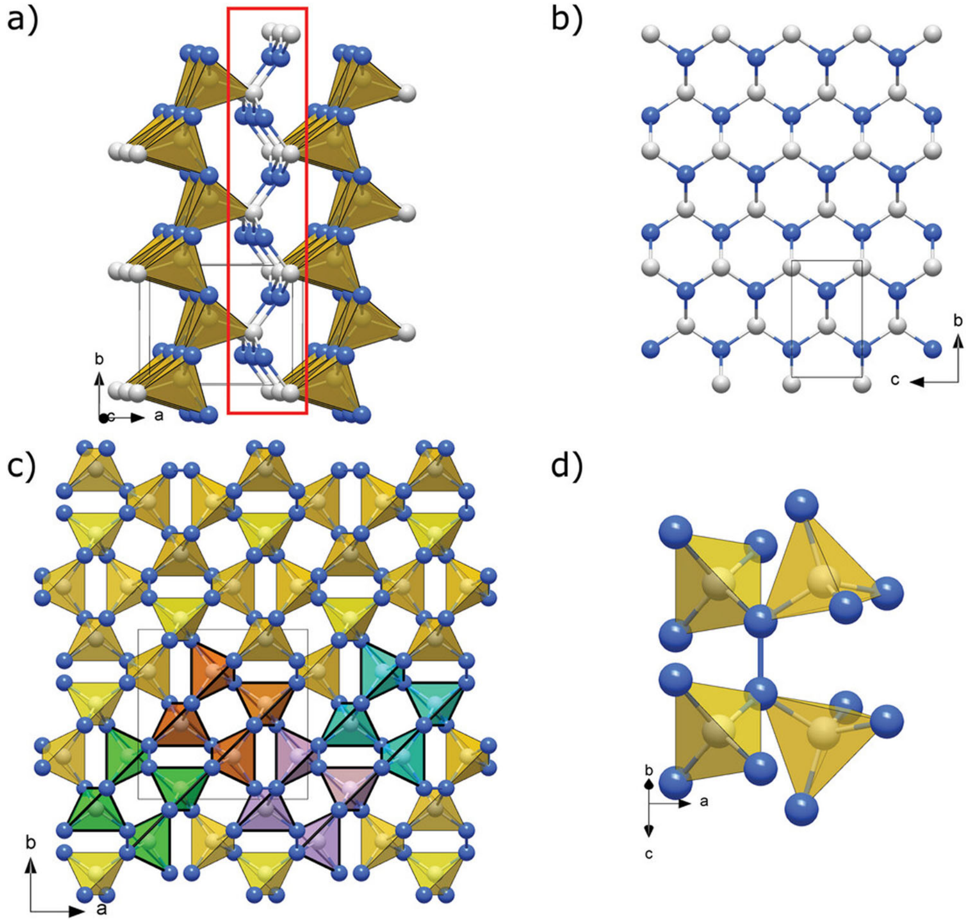

Fig. 3 Crystal structures of *oP*8-CN and *tI*24-CN_2 at 72 and 134 GPa, respectively. (**a**) A polyhedral model of the *oP*8-CN structure built of C-CN_3 tetrahedra. The tetrahedra sharing nitrogen vertices form corrugated layers laying in the *bc* plane, which are connected through carbon apexes of the tetrahedra by triply coordinated nitrogen atoms, as highlighted by the red rectangle. (**b**) A corrugated honeycomb-like net of the 1:1 C:N composition formed by the atoms connecting the layers. (**c**) A polyhedral model of the *tI*24-CN_2 structure (viewed along the c direction) built of corner-sharing CN_4 tetrahedra linked with each other through N_2 dimers. To emphasize that the crystal structure can be understood as repeating units composed of four CN_4 tetrahedra, four of these units are drawn in different colors (green, orange, purple, and teal). d) An example of an N_2 dimer (oriented vertically in the figure) connecting two pairs of corner-sharing CN_4 tetrahedra. Gray and blue spheres represent carbon and nitrogen atoms, respectively. Reproduced from Ref. [15] under Creative Commons License 4.0 (https://creativecommons.org/licenses/by/4.0/). Full details are given in the original publication

compression experiments using lasers with pulse durations in the nanosecond regime. Furthermore, the increased coherence of the X-ray beam at high energies can be exploited for techniques, such as phase contrast imaging, coherent diffraction imaging, and ptychographic imaging, to be applied to new areas of research.

As an example of the new possibilities offered in the field of high-pressure science by the EBS, a study on the synthesis of novel materials under high-pressure conditions was selected. Theoretical studies published 35 years ago [14] had proposed that "hypothetical covalent solids formed between carbon and nitrogen are good candidates for extreme hardness," with a bulk modulus approaching that of diamond, sparking an enormous interest and triggering numerous experimental investigations.

In a very recent study [15], high-pressure X-ray diffraction experiments performed with EBS at the ESRF beamlines ID27 and ID11 enabled the determination of the structure of several novel carbon nitride compounds (*tI*14-C_3 N_4, *hP*126-C_3 N_4, *oP*8-CN, and *tI*24-CN_2), featuring CN_4 tetrahedra. Most importantly, those novel carbon nitrides were found to possess the unique property, among materials synthesized under high pressure (above 100 GPa), of being recoverable in air at ambient conditions.

The extremely high flux of the tightly focused (i.e., $0.47 \times 0.34\ \mu m^2$) hard X-ray beam produced by the EBS on the newly built beamline ID27 beamline (optimized for the EBS), was essential to obtain the necessary high-quality data from submicron-sized crystallites of those low-Z materials [16].

The crystal structures determined for the compounds *oP*8-CN and *tI*24-CN_2 are shown in Fig. 3.

4.2 Dark-field X-ray microscopy

Dark-field X-ray microscopy (DFXM) is a technique designed for the acquisition of three-dimensional (3D) movies of the nanostructure (grains, domains, and dislocations) and the associated local strain within bulk materials. It is analogous to dark-field electron microscopy in that an objective lens magnifies diffracting features of the sample. The use of high-energy synchrotron X-rays, however, means that these microstructural features can be large and deeply embedded. The spatial and angular resolution is on the order of 100 nm and 0.001°, respectively, and full maps can be recorded in seconds to minutes.

The operation principle of DFXM is sketched in Fig. 4 [17, 18]. The diffracted beam passes through an X-ray objective lens, creating a magnified image of a specific region of interest with contrast from local variations in lattice symmetry, orientation, and strain. The sample-to-detector distance is typically 2–6 m, enabling magnification ratios of up to 50, while still maintaining sufficient

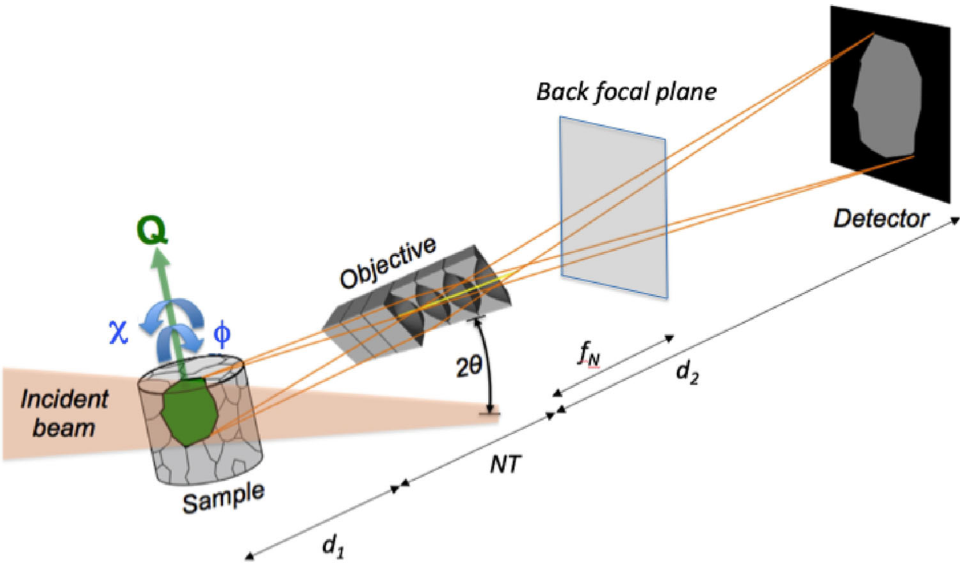

Fig. 4 Principle of dark-field X-ray microscopy. Monochromatic X-rays illuminate a crystalline element of interest, and the diffracted radiation is imaged by means of an X-ray objective and a 2D detector. The objective is here a compound refractive lens (CFL), comprising N lenslets each with a thickness of T. d_1, d_2, f_N are the sample plane-entry of CRL distance, exit-of-CRL to image plane distance, and the focal distance, respectively. Scanning the sample tilt (χ, ϕ) and scattering (2θ) angles facilitate mapping of orientation and axial strain, respectively, while different projections can be obtained by rotating the sample about its scattering vector, **Q**. Reproduced from Ref. [18] under Creative Commons License 4.0 (https://creativecommons.org/licenses/by/4.0/). Full details are given in the original publication

space around the sample for *in situ* sample environments. Maps of the axial strain can be measured by scanning the objective and detector through the scattering angle 2θ, whereas mosaicity maps of local variations in orientation can be similarly obtained by scanning the sample through two orthogonal tilt directions, χ and ϕ.

At the ESRF, the DFXM instrument, originally installed in the ID06-HXM branch [18], now forms the core of the new beamline ID03. Compared to ID06-HXM, ID03 offers optics fully optimized for DFXM, including a pink beam mode and twice the amount of beamtime for users.

Since the restart of the ESRF after the installation of the EBS, the DFXM beamline on ID06-HXM has produced a number of important results, such as a study of the time-evolution of microstructure in heavily deformed ferrite alloys [19], or a high-resolution study of the 3D strain and orientation of grains in Ni superalloys prepared by additive manufacturing [20].

Here, the potential of the EBS for DFXM is illustrated by referring to results from a study of 3D dislocation structures in bulk aluminum [21]. Such studies were not possible with the prevalent technique used so far to investigate dislocation, transmission electron microscopy (TEM), due to the limited penetration power of electron beams. In comparison with other X-ray-based techniques, such as topo-tomography or laminography, DFXM achieves a substantially higher spatial resolution of the microstructure, as the objective both magnifies the image and separates the angular- and direct-space information. The resulting images can thus identify 3D dislocation boundaries with high resolution in both strain and grain orientation. Figure 5 shows a map of several dislocations structures observed at grain boundaries of various orientations. The detailed results for the dislocations parameters (dislocation line vector, Burgers vector) are given in the original publication [21].

4.3 Phase contrast tomography

Several beamlines of the ESRF are fully dedicated to phase contrast tomography (BM05, BM18, and ID19).

A project developed within the ESRF-EBS, BM18, aims at benefiting from the new capabilities of the bending magnet (BM) X-ray source (1.56 T short tripole wiggler) in the new lattice, producing high-energy X-rays (up to 330 keV). The ESRF-EBS represents a significant advancement in X-ray coherence within a storage ring. While remarkable progress has been achieved with undulators in the straight sections of the machine, the most compact X-ray sources, and therefore the highest transverse coherence length, are actually generated using short wigglers installed on the BM ports of the preceding machine. Understanding that coherence is contingent upon both the size of the X-ray source and the distance between the sample and the source, the concept of BM18 has been devised to combine the smallest conceivable X-ray source with the longest feasible beamline at the ESRF, totaling 220 m. Ultimately, BM18 will enable a drastic increase in the scanning of sample sizes (up to 0.7 m in diameter, 2.5 m vertically, and a total weight of 300 kg), while also increasing the sensitivity, especially at high energy. BM18 makes hierarchical imaging possible in a large range of diverse samples, as well as high-throughput imaging of a large series of samples. The main scientific topics that motivated the construction of BM18 are material sciences (for both academic and industrial applications), cultural heritage (especially paleontology which is a long standing tradition at the ESRF), as well as more recently geology, and biomedical imaging.

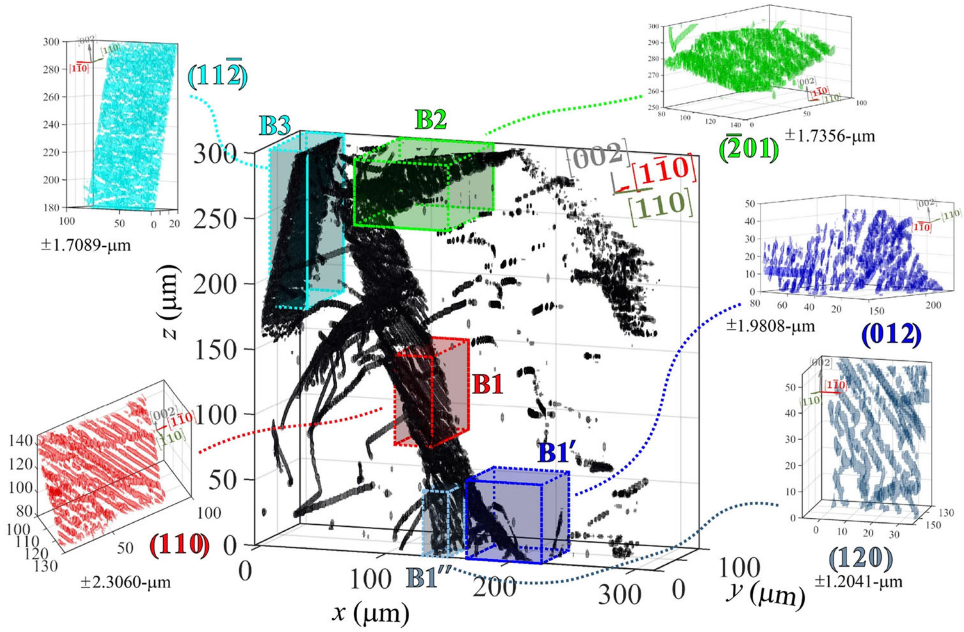

Fig. 5 Assembly several dislocation structures shown, each labeled and outlined in a different color. Shown as inlets are zoom-ins on each boundary to demonstrate its orientation, and demonstrate with the "zoomed-in" view how the single dislocations in that boundary are packed. Reproduced from Ref. [21] under Creative Commons License 4.0 (https://creativecommons.org/licenses/by/4.0/). Full details are given in the original publication

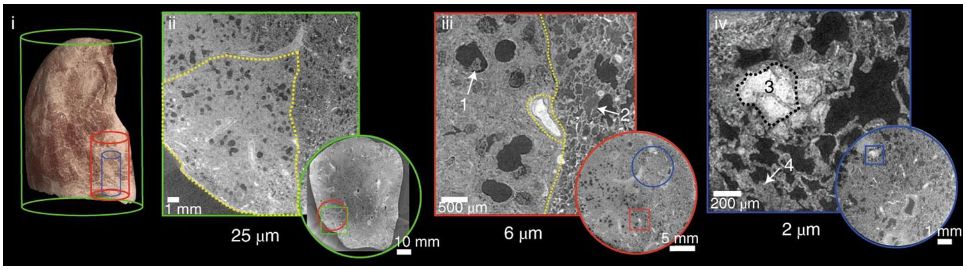

Fig. 6 HiP-CT with 3D image analysis and morphometry in the lung of a patient with COVID-19. (i), A 3D reconstruction from HiP-CT scanning at 25 μm per voxel of the intact upper left lung lobe from the autopsy of a patient who died from COVID-19-related ARDS. High-resolution VOI are shown in red (6.5 μm per voxel) and blue (2.5 μm per voxel). (ii), At 25 μm per voxel, high-intensity regions are observed in the lung periphery. The yellow dotted line delineates a secondary pulmonary lobule. (iii), At 6.5 μm per voxel, heterogeneity in the lung parenchyma included (1) dilated alveolar ducts and diffuse loss of alveolar structural organization and (2) comparatively well-preserved alveolar structure with some edematous changes. (iv), At 2.5 μm per voxel, (3) alveolar obstruction, likely representing clotted blood based on its high intensity, and (4) interstitial thickening of alveolar septa were observed. Reproduced from Ref. [22] under Creative Commons License 4.0 (https://creativecommons.org/licenses/by/4.0/). Full details are given in the original publication

Below, we present some examples of recent experiments of phase contrast tomography applied to anatomical samples using EBS.

The restart of the ESRF after the construction of the EBS fell into the COVID-19 pandemic. The immediate utilization of the EBS enabled the examination of the lungs of patients who had recently deceased to COVID-19. This study aimed to obtain further insights into the pandemic's impact on the respiratory system [22].

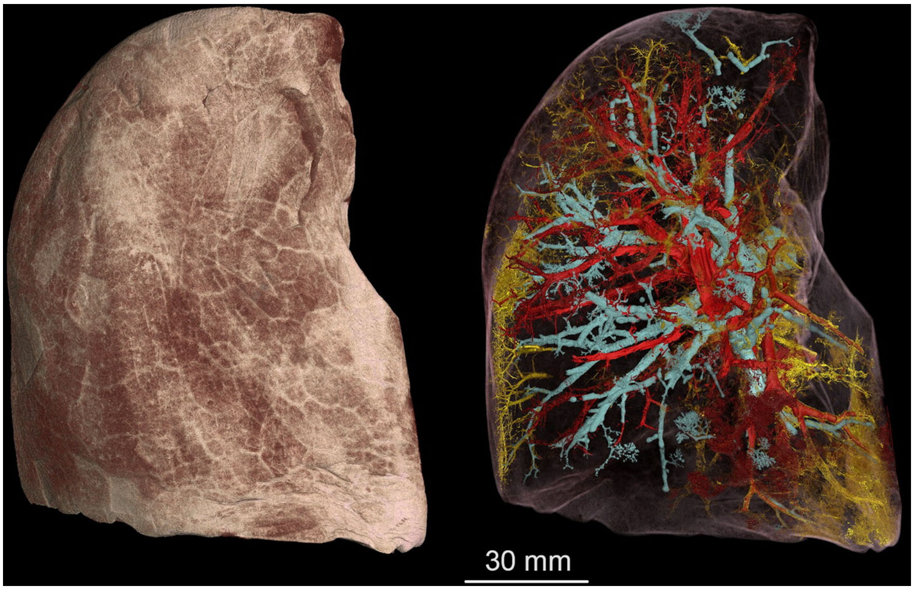

Fig. 7 The lung of a man who died from COVID-19 is depicted by a new type of scan showing open blood vessels in red, blocked blood vessels in yellow, and air spaces in cyan. ©Paul Tafforeau/ESRF

To assess the suitability of hierarchical phase contrast tomography (HiP-CT) to detect changes in SARS-CoV-2-infected lungs, tomographic images have been acquired on BM05 on an intact upper right lung lobe acquired from the autopsy of a 54-year-old male patient who died from COVID-19-related Acute Respiratory Distress Syndrome (ARDS) (Fig. 6) [22]. Figure 6 shows hierarchical phase contrast tomography (HiP-CT) images of the lung at various levels of details. High magnification at 2 μm per voxel (Fig. 6iv) revealed alveolar obstruction (3) and interstitial thickening of alveolar septa (4), providing valuable insight into the effect of the SARS-CoV-2 virus. Further images are shown in Fig. 7.

This work laid the foundation for an ambitious project, the Human Organ Atlas Project [23], bringing together eight institutions under the leadership of the University College London for the creation of an open-access database of multi-resolution tomographic scans of intact human organs. The large sample stage currently being installed on beamline BM18 [24] will ultimately enable multi-resolution scans of entire human bodies.

5 Perspectives and new challenges

After completion of the EBS, the ESRF will continue its evolution in order to best fulfill its double mission: (i) producing X-ray synchrotron radiation with the highest possible performance in terms of brilliance, transverse coherence, and stability; and (ii) providing a portfolio of state-of-the-art beamlines and ancillary support services to the ESRF user community for the optimum exploitation of the ESRF-EBS for fundamental and applied science as well as for industrial clients.

5.1 X-ray source

With the successful delivery of the ESRF-EBS, the primary focus is on the reliable operation and preventive maintenance of the accelerator complex. This comprises a further optimization of the machine performance and operation for users, a gradual increase of bunch current for the timing mode in 16-bunch operation, corrective actions on some weak parts of the accelerator complex to increase reliability, continued hardware upgrades, and procurement of spares.

In addition, several major investments whose objective is to secure and further improve the operation performance will be made, including: (i) the production and installation of new insertion devices together with an update of their control software; (ii) the replacement of the klystrons with solid-state amplifiers as the power source of the RF system in the storage ring, to ensure and consolidate the long-term operation with high reliability and stability; (iii) the refurbishment of the injector, especially the booster, to improve injection efficiency and reduce unwanted effects of perturbations occurring during the beam injection; (iv) the design and implementation of a 4th harmonic RF system for bunch lengthening, in order to reduce the electron density (the lower beam size in the EBS resulted in a density increase), thereby improving the Touschek lifetime of the electron beam [25].

5.2 Beamlines

The ESRF beamline construction and refurbishment program of the beamlines is almost completed with essentially all beamlines back in user operation with the exception of EBSL1, the new coherence beamline, and the biomedical beamline ID17 that are both currently on hold. The beamline refurbishments to be concluded in 2024 concern (i) ID21—the X-ray microscopy beamline, (ii) ID24-DCM—high-brilliance XAS beamline, (iii) ID14—nuclear resonance scattering, (iv) ID26—X-ray absorption and emission spectroscopy beamline. Future refurbishments are planned for beamlines that have not undergone a major refurbishment during Phase I or II of the upgrade such as ID11—materials science beamline, ID13—microfocus beamline, and ID28—inelastic scattering II, but also ID12—circular polarization and ID10—surface science. Following the successful commissioning of the ESRF spectroscopy double-crystal monochromator (DCM) on ID21—X-ray microscopy, BM23—X-ray absorption spectroscopy, and ID24—high-brilliance X-ray absorption spectroscopy, further DCMs shall be deployed on BM23, ID16B—nano-analysis, and ID26—X-ray absorption and emission.

5.3 Data strategy

The data challenge relates to a drastic increase in the volume of detector raw data incurred by a variety of factors on the instrumentation side (higher intensity X-ray beams, detectors with a larger number of smaller pixels and/or operating at higher frame rates), as well as on the scientific side (multidimensional datasets with complex information content). This leads not only to an increased need for data storage and archiving capacity, but also to a large increase in the request for real-time and post-processing capacity of big data volumes.

The driving factors include the improvement of the overall data acquisition process (faster, more reliable); the extensive online monitoring of incoming data; the development of data triage for irrelevant datasets; the creation of tools for data compression at the source to limit the burden on the downstream part of the IT infrastructure; the provision of sufficient retention time for data on disk to facilitate offline computing; the support of users in processing ESRF data to maintain a high level of scientific publications despite the increasing complexity of datasets; the provision of tools and hardware for archiving datasets over a 10-year period. The ESRF data policy, complying with the FAIR principles (Findable, Accessible, Interoperable, and Reusable), is described in Ref. [26].

5.4 User program

Recognizing the potential to expand the ESRF-EBS's international scientific reach by developing new user communities, especially from the largely untapped pool of nonexpert users, the ESRF launched its new Community Proposals access modes in 2022. These access modes include Block Allocation Group—BAG (non-MX) and HUB program proposals [27].

As a start, the ESRF has launched three pilot projects in areas of interest to the ESRF user community: historical materials, shock experiments, and batteries. Each pilot project represents a new access route based on community access granted to a larger group of principal investigators (PIs) or a consortium of applicants. More specifically:

- *Science-driven Block Allocation Group (BAG)* a specific science community selects the scientifically most promising experiments fostering (i) collaboration and (ii) the most effective use of the available beamtime.
- *Technique-driven BAG* the entire user community of a specific technique selects the scientifically most promising experiments fostering (i) collaboration, (ii) pooling of community expertise and resources, and (iii) the most effective use of the available beamtime.
- *Science HUB* the ESRF channels a part of its resources into a science hub in selected areas of the highest societal relevance. The aim is again to foster (i) collaboration and (ii) maximize the impact of the use of the ESRF resources.

In the first official round of Community Proposals, the Human Organ Atlas HUB (HOAHub) was approved in 2023 (see above).

In addition, new access mode pilots for rapid and coordinated access have been developed in 2023 to create additional opportunities for the user community. Rapid access modes are designed to allow users to access ESRF beamlines quickly and easily, typically for short experiments. Coordinated access targets a specific community in the frame of a grant that needs access to analytical facilities (in addition to conventional laboratory equipment).

Supplementary Information The online version contains supplementary material available at https://doi.org/10.1140/epjp/s13360-024-05719-6.

Acknowledgements The authors want to thank the entire ESRF staff, whose expertise and commitment made the EBS project possible.

Funding This work has been done as part of the STREAMLINE project that has received funding from the European Union's Horizon 2020 research and innovation program under grant agreement No 870313.

Data Availability Statement This article refers exclusively to the results of the publications listed below. There are no new data associated available.

References

1. R. Haensel, European synchrotron radiation facility. Acta Phys. Polonica A **82**(1), 33–36 (1992). https://doi.org/10.1016/0168-9002(88)90360-9
2. Y. Farge, L'Élaboration du projet ESRF. Histoire de la Recherche Contemporaine **1**(1), 1–10 (2012)
3. K.C. Cramer, Lightening Europe: establishing the european synchrotron radiation facility (ESRF). Hist. Technol. **33**(4), 396–427 (2017). https://doi.org/10.1080/07341512.2018.1489762
4. The European Light Source - Science and Technology Programme 2008-2017 (The Purple Book), ESRF (Grenoble), (2007). https://www.esrf.fr/files/live/sites/www/files/about/upgrade/documentation/ESRF-SciTechProg2008-2017.pdf
5. ESRF Upgrade Programme Phase II (201-2022) - Technical Design Study (The Orange Book), ESRF (Grenoble), (2015). https://www.esrf.fr/files/live/sites/www/files/about/upgrade/documentation/ESRF-orange-book.pdf
6. ESRF Upgrade Programme Phase II (2015-2019) White Paper, ESRF (Grenoble) (2013). https://www.esrf.fr/files/live/sites/www/files/about/upgrade/documentation/whitepaper-upgrade-phaseII.pdf
7. D. Einfeld, J. Schaper, M. Plesko, Design of a diffraction limited light source (DIFL). Proc. Part. Accelerat. Conf. **1**, 177–179 (1995). https://doi.org/10.1109/PAC.1995.504602
8. D. Einfeld, Multi-bend achromat lattices for storage ring light sources. Synchrotron Radiat. News **27**(6), 4–7 (2014). https://doi.org/10.1080/08940886.2014.970929
9. J.C. Biasci, J.F. Bouteille, N. Carmignani, J. Chavanne, D. Coulon, Y. Dabin, F. Ewald, L. Farvacque, L. Goirand, M. Hahn, J. Jacob, G. LeBec, S. Liuzzo, B. Nash, H. Pedroso-Marques, T. Perron, E. Plouviez, P. Raimondi, J.L. Revol, K. Scheidt, V. Serrière, A low-emittance lattice for the ESRF. Synchrotron Radiat. News **27**(6), 8–12 (2014). https://doi.org/10.1080/08940886.2014.970931
10. P. Raimondi, N. Carmignani, L.R. Carver, J. Chavanne, L. Farvaque, G. Le bec, D. Martin, S.M. Liuzzo, T. Perron, S. White, Commissioning the hybrid multibend achromat lattice at the European synchrotron radiation facility. Phys. Rev. Accel. Beams (2021). https://doi.org/10.1103/PhysRevAccelBeams.24.110701
11. P. Raimondi, C. Benabderrahmane, P. Berkvens, J.-C. Biasci, P. Borowiec, J.-F. Bouteille, T. Brochard, N.B. Brookes, N. Carmignani, L.R. Carver, J.-M. Chaize, J. Chavanne, S. Checchia, Y. Chushkin, F. Cianciosi, M. Di Michiel, R. Dimper, A. D'Elia, D. Einfeld, F. Ewald, L. Farvacque, L. Goirand, L. Hardy, J. Jacob, L. Jolly, M. Krisch, G. Le Bec, I. Leconte1, S.M. Liuzzo, C. Maccarrone, T. Marchial, D. Martin, M. Mezouar, C. Nevo, T. Perron, E. Plouviez, H. Reichert, P. Renaud, J.-L. Revol, B. Roche, K.-B. Scheidt, V. Serrière, F. Sette, J. Susini, L. Torino, R. Versteegen, S. White, and F. Zontone, The Extremely Brilliant Source storage ring of the European Synchrotron Radiation Facility. Comm. Phys. **6:82**, 1–11 (2023). https://doi.org/10.1038/s42005-023-01195-z
12. P. Raimondi, *The ESRF low emittance upgrade*, Proceedings of the 7th International Particle Accelerator Conference – IPAC2026, Busan (2016). https://doi.org/10.18429/JACoW-IPAC2016-WEXA01
13. P. Raimondi, S.M. Liuzzo, Towards a diffraction limited light source. Phys. Rev. Accel. Beams (2023). https://doi.org/10.1103/PhysRevAccelBeams.26.021601
14. A.Y. Liu, M.L. Cohen, Prediction of new low compressibility solids. Science **245**, 841 (1989). https://doi.org/10.1126/science.245.4920.841
15. D. Laniel, F. Trybel, A. Aslandukov, S. Khandarkhaeva, T. Fedotenko, Y. Yin, N. Miyajima, F. Tasnádi, A.V. Ponomareva, N. Jena, F.I. Akbar, B. Winkler, A. Néri, S. Chariton, V. Prakapenka, V. Milman, W. Schnick, A.N. Rudenko, M.I. Katsnelson, I.A. Abrikosov, L. Dubrovinsky, N. Dubrovinskaia, Synthesis of ultra-incompressible and recoverable carbon nitrides featuring CN4 Tetrahedra. Adv. Mater. **36**(230830), 1–12 (2024). https://doi.org/10.1002/adma.202308030
16. M. Mezouar, G. Garbarino, S. Bauchau, W. Morgenroth, K. Martel, S. Petitdemange, P. Got, C. Clavel, A. Moyne, H.-P. Van Der Kleij, A. Pakohmova, B. Wehinger, M. Gerin, T. Poreba, L. Canet, A. Rosa, A. Forestier, G. Weck, F. Datchi, M. Wilke, S. Jahn, D. Andrault, L. Libon, L. Pennacchioni, G. Kovalskii, M. Herrmann, D. Laniel, H. Bureau, The high flux nano-X-ray diffraction, fluorescence and imaging beamline ID27 for science under extreme conditions on the ESRF Extremely Brilliant Source. High Press. Res. **44**(3), 171–198 (2024). https://doi.org/10.1080/08957959.2024.2363932
17. H. Simons, A. King, W. Ludwig, C. Detlefs, W. Pantleon, S. Schmidt, F. Sthr, I. Snigireva, A. Snigirev, H.F. Poulsen, Dark-field X-ray microscopy for multiscale structural characterization. Nature Comm. **6**(6098), 1–6 (2015). https://doi.org/10.1038/ncomms7098
18. M. Kutsal, P. Bernard, G. Berruyer, P.K. Cook, R. Hino, A.C. Jakobsen, W. Ludwig, J. Ormstrup, T. Roth, H. Simons, K. Smets, J.X. Sierra, J. Wade, P. Wattecamps, C. Yildirim, H.F. Poulsen, C. Detlefs, The ESRF dark-field x-ray microscope at ID06. IOP Conf. Series: Mater. Sci. Eng. (2019). https://doi.org/10.1088/1757-899X/580/1/012007
19. C. Yildirim, N. Mavrikakis, P.K. Cook, R. Rodriguez-Lamas, M. Kutsal, H.F. Poulsen, C. Detlefs, 4D microstructural evolution in a heavily deformed ferritic alloy: a new perspective in recrystallisation studies. Scripta Mater. **214**(114689), 1–7 (2022). https://doi.org/10.1016/j.scriptamat.2022.114689
20. Y. Chen, Y.T. Tang, D.M. Collins, S.J. Clark, W. Ludwig, R. Rodriguez-Lamas, C. Detlefs, R.C. Reed, P.D. Lee, P.J. Withers, C. Yildirim, High-resolution 3D strain and orientation mapping within a grain of a directed energy deposition laser additively manufactured superalloy. Scripta Mater. **234**(115579), 1–6 (2023). https://doi.org/10.1016/j.scriptamat.2023.115579
21. C. Yildirim, H.F. Poulsen, G. Winther, C. Detlefs, P.H. Huang, L.E. Dresselhaus-Marais, Extensive 3D mapping of dislocation structures in bulk aluminum. Sci. Rep. **13**(3834), 1–11 (2023). https://doi.org/10.1038/s41598-023-30767-w
22. C.L. Walsh, P. Tafforeau, W.L. Wagner, D.J. Jafree, A. Bellier, C. Werlein, M.P. Khnel, E. Boller, S. Walker-Samuel, J.L. Robertus, D.A. Long, J. Jacob, S. Marussi, E. Brown, N. Holroyd, D.D. Jonigk, M. Ackermann, P.D. Lee, Imaging intact human organs with local resolution of cellular structures using hierarchical phase-contrast tomography. Nat. Methods **18**, 1532–1541 (2021). https://doi.org/10.1038/s41592-021-01317-x
23. *Human Organ Atlas*, https://human-organ-atlas.esrf.eu/
24. F. Cianciosi, A.L. Buisson, P. Tafforeau, and P. Van Vaerenbergh, *BM18, the new ESRF-EBS beamline for hierarchical phase-contrast tomography*, Proceedings of the 11th International Conference on Mechanical Engineering Design of Synchrotron Radiation Equipment and Instrumentation, 1–5 (2021). https://doi.org/10.18429/JACoW-MEDSI2020-MOIO02
25. A. D'Elia, V. Serrière, J. Jacob, and X. Zhu, *Design of 4th harmonic RF cavities for ESRF-EBS*, in *Proc. IPAC'21*, Campinas, SP, Brazil, May 2021, pp. 1031–1033. https://doi.org/10.18429/JACoW-IPAC2021-MOPAB332

26. V. Favre-Nicolin, A. Gtz, M. Krisch, and G. Martinez-Criado (2024), *ESRF Data Policy 2024 (Version 1)*, European Synchrotron Radiation Facility, Grenoble (2024). https://www.esrf.fr/files/live/sites/www/files/Infrastructure/Computing/ESRF-data-policy_20240101.pdf
27. J. McCarthy, H. Reichert, ESRF prepares new user access modes. Synchrotron Radiat. News **35**, 52–54 (2022). https://doi.org/10.1080/08940886.2022.2064150